photochem

MDPI

Article

Facile Doping of 2,2,2-Trifluoroethanol to Single-Walled Carbon Nanotubes Electrodes for Durable Perovskite Solar Cells

Naoki Ueoka [1], Achmad Syarif Hidayat [1], Hisayoshi Oshima [2], Yoshimasa Hijikata [3] and Yutaka Matsuo [1,2,*]

[1] Department of Chemical Systems Engineering, Graduate School of Engineering, Nagoya University, Furo-cho, Chikusa-ku, Nagoya 464-8603, Japan; ueoka.naoki.z1@f.mail.nagoya-u.ac.jp (N.U.); achmad.syarif.hidayat.w3@s.mail.nagoya-u.ac.jp (A.S.H.)
[2] Institute of Materials Innovation, Institutes for Future Society, Nagoya University, Furo-cho, Chikusa-ku, Nagoya 464-8603, Japan; oshima.hisayoshi.c3@f.mail.nagoya-u.ac.jp
[3] Advanced Research and Innovation Center, DENSO CORPORATION, 1-1, Showa-cho, Kariya 448-8661, Japan; yoshimasa.hijikata.j7t@jp.denso.com
* Correspondence: matsuo.yutaka.h7@f.mail.nagoya-u.ac.jp

Abstract: Perovskite solar cells with an indium tin oxide (ITO)/SnO_2/$CH_3NH_3PbI_3$/Spiro-OMeTAD/2,2,2-trifluoroethanol (TFE) doped single-walled carbon nanotube (SWCNT) structure were developed by dropping TFE onto SWCNTs, which replaced the metal back electrode, and a conversion efficiency of 14.1% was achieved. Traditionally, acidic doping of the back electrode, SWCNT, has been challenging due to the potential damage it may cause to the perovskite layer. However, TFE has facilitated easy doping of SWCNT as the back electrode. The sheet resistance of the SWCNTs decreased and their ionization potential shifted to deeper levels, resulting in improved hole transport properties with a lower barrier to carrier transport. Furthermore, the Seebeck coefficient (*S*) increased from 34.5 μV/K to 73.1 μV/K when TFE was dropped instead of EtOH, indicating an enhancement in the behavior of p-type charge carriers. It was observed that hydrophilic substances adhered less to the SWCNT surface, and the formation of PbI_2 was suppressed. These effects resulted in higher conversion efficiency and improved solar cell performance. Furthermore, the decrease in conversion efficiency after 260 days was suppressed, showing improved durability. The study suggests that combining SWCNTs and TFEs improves solar cell performance and stability.

Keywords: single-walled carbon nanotube; perovskite solar cells; 2,2,2-trifluoroethanol; durability

Citation: Ueoka, N.; Hidayat, A.S.; Oshima, H.; Hijikata, Y.; Matsuo, Y. Facile Doping of 2,2,2-Trifluoroethanol to Single-Walled Carbon Nanotubes Electrodes for Durable Perovskite Solar Cells. *Photochem* **2024**, *4*, 319–333. https://doi.org/10.3390/photochem4030019

Received: 29 May 2024
Revised: 4 July 2024
Accepted: 10 July 2024
Published: 14 July 2024

1. Introduction

Perovskite solar cells are known for their high light absorption rates, light weight, and flexibility. Since they were first reported in 2009, the performance of perovskite solar cells has improved and research into their practical application has progressed significantly [1–3]. A notable feature of these solar cells is their flexibility and lightweight design, which has been difficult to achieve with conventional silicon solar cells. Perovskite solar cells have the unique advantage of being able to be installed in a diverse range of locations, such as building windows and cars. This expands their potential for new application areas, which has been a challenge for conventional solar cells. As a result, perovskite solar cells have opened new avenues for expanding the use of renewable energy technology [4–6]. Power generation efficiencies of more than 20% have already been achieved in single cells of perovskite solar cells [7–9]. This is very efficient and outperforms conventional solar cells. Therefore, perovskite solar cells with higher power generation efficiency and stability are expected to be put into practical use. A common perovskite crystal, $CH_3NH_3PbI_3$ ($MAPbI_3$), has optical absorption properties in the visible region, with a band gap of 1.6 eV. This property effectively absorbs a portion of the solar spectrum, enabling efficient solar power generation. Thus, perovskite solar cells can perform well in various environments and may contribute to the widespread use of renewable energy [10–15].

Perovskite solar cells using single-walled carbon nanotubes (SWCNTs) have attracted much attention because of their potential for flexibility and low cost while maintaining high power generation efficiency. Usually, metals such as gold, silver, and copper are used for the backside electrodes of organic and perovskite solar cells [16–19]. However, these metals require vacuum deposition for fabrication and they are expensive. Previous studies have reported that these metal atoms can diffuse inside the stacks and break down the perovskite crystals [20]. The substrate material must have high transparency and electrical conductivity. The materials commonly used for this purpose are indium tin oxide (ITO) and fluorine-doped tin oxide (FTO). However, ITO requires the use of indium, which is a rare metal and increases the cost of solar cells. Moreover, these materials are not suitable for applications that require flexible cells. Therefore, there is a need to develop flexible and cost-effective substrate materials. SWCNTs are of interest here because of their excellent properties, flexibility, and electrical conductivity. SWCNTs have metallic and semiconducting types, which can be confirmed by optical analysis. The optical absorption wavelengths of the metallic and semiconducting types are observed simultaneously in SWCNT thin films, suggesting a mixture of the two types [21]. The Seebeck coefficient (S) measures the magnitude of the thermoelectric effect and reflects the amount of charge carriers (electrons and holes) generated in a material due to a temperature gradient. Specifically, it is the change in voltage (ΔV) due to a temperature difference divided by the unit temperature difference (ΔT). The Seebeck coefficient is usually expressed in units of Boltzmann's constant (k) or elementary charge (e). The following is the definition of the Seebeck coefficient (S) [22,23]:

$$S = -\left(\frac{\Delta V}{\Delta T}\right) \quad (1)$$

For n-type thermoelectric materials, electrons generated on the high-temperature side flow to the low-temperature side due to the diffusion force caused by the difference in electron concentration, resulting in high potential on the high-temperature side and low potential on the low-temperature side. As a result, the Seebeck coefficient S of n-type semiconductors has a negative sign. On the other hand, in p-type semiconductors, the electron flow is in the opposite direction, and S has a positive sign. It has been experimentally confirmed that SWCNTs usually exhibit p-type semiconductor properties due to oxygen [24]. p-Type doping can be achieved through the use of acids like HNO_3. Acid treatment has been observed to transform the normal state of SWCNTs into a p-type semiconductor, resulting in the removal of impurities, decreased inter-bundle junction resistance, and decreased sheet resistance [25]. This process offers the ability to control the Seebeck coefficient and enhance the performance of SWCNTs used as thermoelectric materials.

In a 2017 study, we reported a conversion efficiency of 9.8% for inverted perovskite solar cells with a CNT/poly(3,4-ethylenedioxythiophene) polystyrene sulfonate (PEDOT:PSS)/$CH_3NH_3PbI_3$/phenyl-C61-butyric acid methyl ester (PCBM)/Al structure using SWCNTs modified with HNO_3 as a p-dopant [26]. Interestingly, PCBM was found to form an electron-selective charge-selective layer on SWCNTs in that study. This discovery led to the development of a new solar cell structure combining a CNT transparent electrode (anode) and a CNT backside electrode (cathode) [26]. Unlike the conventional metal and metal oxide electrodes, CNT electrodes provide unique properties such as flexibility and stability. In 2019, we also reported that the conductivity and work function were adjusted by applying vapor doping with trifluoromethanesulfonic acid (TFMS), a strong acid, to SWCNTs. Solar cells with a ITO/SnO_2/formamidinium (CH_5N_2)$CsPbI_3$/Spiro-OMeTAD/CNT doped with TFMS achieved a high-power conversion efficiency of 17.6% [27]. Formamidinium is known to be thermally more stable than methylammonium [28]. Partial doping techniques have also utilized alkali metal elements such as cesium and sodium, which can improve the crystal structure of $MAPbI_3$ and control impurities in perovskite solar cells, thereby improving power generation efficiency [29,30]. Researchers have noted that while strong acids can be used as p-type dopants, human health and industrial considerations have necessitated the search for weaker dopants; MoO_3 is also used as a p-type dopant

and has been suggested to shift the work function of SWCNTs to deeper levels [31,32]. However, MoO_3 requires complicated fabrication techniques because it must be deposited by thermal eVaporation rather than solution-coating. $AuCl_3$ and Nafion polymeric acid can maintain the conductivity of SWCNTs without sacrificing their transparency, allowing their application in organic solar cells [33,34]. There are issues with relatively safe gold chloride (AuCl) dopants that can degrade electrical performance, and with Nafion solution containing water, perovskite crystals can easily be damaged. Thus, dopant materials have been limited in perovskite solar cells because damage to the perovskite crystals with respect to the p-doping of SWCNTs on back electrode must be considered.

In this study, we report a mild p-doping methodology using 2,2,2-trifluoromethanol (TFE) which can be applied to enhance the performance of SWCNT film electrodes eVen after transferring them onto perovskite/hole-transport layers. In devices with a structure of ITO/SnO_2/$MAPbI_3$/Spiro-OMeTAD/TFE-doped SWCNT, fluorine atoms of TFE play a significant role in weakening the hydrogen bonds of water molecules and enhancing hydrophobic interactions. [35]. TFE is liquid under normal conditions, and doping can be easily applied by spin-coating. Notably, its acidity is considerably lower than that of HNO_3 and TFMS, as shown by their acid dissociation constants: TFMS (pKa = −14) > HNO_3 (pKa = −1.4) > TFE (pKa = 12.4) > EtOH (pKa = 15.9). The application of TFE decreased in the sheet resistance of SWCNTs and shift their work function to a slightly deeper level. This improvement resulted in improved open-circuit voltage (V_{OC}) and fill factor (FF), and power conversion efficiency increased from 13.0% to 14.1% after TFE doping for SWCNTs with transmittance of T_{550nm} = 41%. When we used thicker SWCNT films with transmittance of T_{550nm} = 28%, the rate of decrease in conversion efficiency after 30 days was smaller than devices using SWCNT films with T_{550nm} = 41%, indicating that the perovskite solar cells became more stable with TFE-doped thicker SWCNT back electrodes. Furthermore, it was confirmed that the stability effect of TFE doping persisted eVen after 260 days. The findings of this study underscore the potential benefits of utilizing TFE in enhancing the performance and stability of perovskite solar cells equipped with SWCNT back electrodes.

2. Experimental

2.1. Synthesis and Fabrication of Patterned SWCNTs Films

Floating catalyst chemical vapor deposition was employed for single walled carbon nanotubes (SWCNTs) synthesis [36]. During the synthesis of SWCNTs, CH_4 was utilized as the carbon source, while ferrocene and solid sulfur were used as Fe catalyst and a reaction promoter. Hydrogen was added to suppress CH_4 polymerization. The carrier gas was nitrogen. The synthesis process was carried out in a quartz tube with a diameter of 50 mm at a temperature of 950 °C. To form a electrode-sized SWCNTs film, SWCNTs in the reaction gas were collected by a membrane filter [37] attached with a patterned SUS mask. The mask was inserted the downstream side of the filter to prevent the SWCNTs' deposition on the mask surface [38].

2.2. Fabrication of the Perovskite Solar Cells

Indium-tin oxide patterned glass substrates (15 mm × 15 mm, ~10 Ω/sq) were cleaned in an ultrasonic bath with ethanol and acetone and dried under nitrogen gas. Then, ITO substrates were treated with UV/O_3 for 15 min. The SnO_2 precursor solutions were prepared from Tin(IV) oxide, 15% in H_2O colloidal dispersion (Alfa Aesar, Ward Hill, MA, America, 200 μL) with deionized water (600 μL) was spin-coated on the ITO substrate at 3000 rpm for 30 s, and the coated substrate was then annealed at 150 °C for 30 min. Then, the substrates were transferred into a N_2-filled glove box after treatment with UV/O_3.

The perovskite precursor solution was prepared by dissolving CH_3NH_3I (Sigma-Aldrich, St. Louis, MI, USA, 122 mg) and PbI_2 (Tokyo Chemical Industries, Tokyo, Japan, 355 mg) in a mixture of DMF (Sigma-Aldrich, 490 μL) and DMSO (Sigma-Aldrich, 55 μL) The perovskite solution was spin-coated at 4000 rpm for 20 s. A total of 120 μL of an-

tisolvent chlorobenzene was slowly dripped onto the substrate 7 s after the start of the spin-coating process [39]. The transparent film was subsequently annealed at 100 °C for 10 min. The SWCNTs were transferred onto the perovskite layer after removing the substrate from the outside and spin-coating with Spiro-OMeTAD at 4000 rpm for 20 s in a glove box. A solution of spiro-OMeTAD (Wako Pure Chemical Industries, Osaka, Japan, 45 mg) in chlorobenzene (Sigma-Aldrich, 500 µL) was mixed with a solution of lithium bis(tri-fluoromethylsulfonyl)imide (Li-TFSI; Sigma-Aldrich, 130 mg) in acetonitrile (Sigma-Aldrich, 250 µL). The former solution with 4-tert-butylpyridine (Sigma-Aldrich, 18 µL) was mixed with the Li-TFSI solution (11 µL). Finally, the TFE solution was spin-coated at 4000 rpm for 20 s onto the SWCNT electrodes. Silver (Ag) electrodes were eVaporated as top electrodes using a patterning mask for the reference device. Layered structures of the prepared photovoltaic devices are denoted as ITO/SnO_2/perovskite/spiro-OMeTAD/SWCNT(TFE). The prepared perovskite photovoltaic devices were stored at 25 °C and ~30% humidity.

2.3. Characterizations

Solar simulated AM 1.5G sunlight was generated with a HAL-C100 solar simulator (Asahi Spectra Co., Tokyo, Japan) calibrated to give 100 mWcm^{-2} using an ML-01 silicon pyranometer (Eko Instrument Co., Ltd., Tokyo, Japan) The current density–voltage (*J–V*) curves were recorded with Keysight, B2900, having set the integration time (NPLC) and measurement delay (ms) to 1 and 0.01, respectively. A metal aperture with an area of 0.04 cm^2 was applied to confine the active area and light shed from ITO side. The incident-photon-to-current conversion efficiency (IPCE) was measured using an MLS-1510 monochromator (Asahi Spectra Co., Japan) with a model 1918-R power meter. A source measurement unit recorded the current at each specific wavelength. A FLAME-S miniature Spectrometer (OptoSirius Co., Tokyo, Japan) was used to measure the absorption of the perovskite devices. The Fermi levels were measured by Riken Keiki photoelectron yield spectroscopy AC-2. Sheet resistance of the SWCNT electrodes was measured using a four-point probe, and a digital multimeter (DL-1060, TEXIO TECHNOLOGY Co., Kanagawa, Japan). SEM images were obtained using field emission-scanning electron microscopy equipped with EDS (S-4800, Hitachi High-Tech Co., Tokyo, Japan). The X-ray photoelectron spectroscopy (XPS, ESCALAB 250Xi, Thermo Scientific, Waltam, MA, USA) was used to analyze the chemical state of SWCNT. Raman spectra were taken using a confocal Raman microscope system, using a 1800 l/mm grating and $\lambda_{ex.532\,nm}$ (Renishaw, inVia reflex). Seebeck coefficients were measured under the atmosphere using a commercial measurement system (ZEM-2, Advanced Riko, Inc., Kanagawa, Japan). The crystalline structure of $CH_3NH_3PbI_3$ was characterized with an X-ray diffractometer (XRD, ATX-G, Rigaku, Tokyo, Japan) equipped with Cu-kα (λ = 0.15456 nm) radiation. The water contact angle measurements were conducted using the $\theta/2$ method.

3. Results and Discussion

J–V characteristics under AM1.5 simulated sunlight (100 mW cm^{-2}) and incident photon-to-electron conversion efficiency spectra of the present perovskite solar cells with SWCNT electrodes are shown in Figures 1a and 1b, respectively. The measured photovoltaic parameters of the perovskite solar cells are summarized in Table 1. The standard cell with Ag electrodes provided a short-circuit current density (J_{SC}) of 24.2 mA cm^{-2}, V_{OC} of 0.948 V, FF of 0.711, and power conversion efficiency (η) of 16.4%. When the electrode had SWCNT transmittance of T_{550nm} = 41%, the cell achieved η of 13.0%, slightly lower than the value of silver electrodes due to the light transmission; Figure S1 shows *J–V* curves for cells with SWCNT transmittance of T_{550nm} = 41% and T_{550nm} = 28%. A slightly higher η was observed for the 41% transmittance case, whereas a lower V_{OC} was observed for the 28% transmittance case, likely due to charge recombination at the 28% transmittance film. Therefore, lowering the transmittance of SWCNTs is expected to hinder electron and hole transport within the nanotube films. V_{OC} is increased from 0.901 V to 0.941 V by doping

TFE to SWCNT transmittance of T_{550nm} = 41%, improving η from 13.0% to 14.1%. The effect of TFE doping was clearly observed from the statistical analysis of the five samples (Figure S2). The EQE results corresponded well to the J_{SC} values obtained from the *J*–*V* characteristics. In Figure S3, the IQE spectrum can be calculated from the EQE results and the light absorption efficiency [40–42]. Ignoring the reflectance, a comparison between the Ag electrode and the TFE-doped SWCNT electrode revealed a surprising result: despite light transmission around 400 nm for the SWCNT electrode, the IQE was 85%, which is almost the same as the 88% of the Ag electrode. The energy gap of Spiro-OMeTAD is 2.94 eV, allowing it to absorb light within this wavelength range and significantly influence hole transport [43,44]. Moreover, the hole capture efficiency can be determined by the IQE [45–47]. Despite the lower light absorption efficiency at a wavelength of 400 nm, the IQE of SWCNT was almost the same as that of Ag. This suggests that the hole capture efficiency of SWCNT is superior.

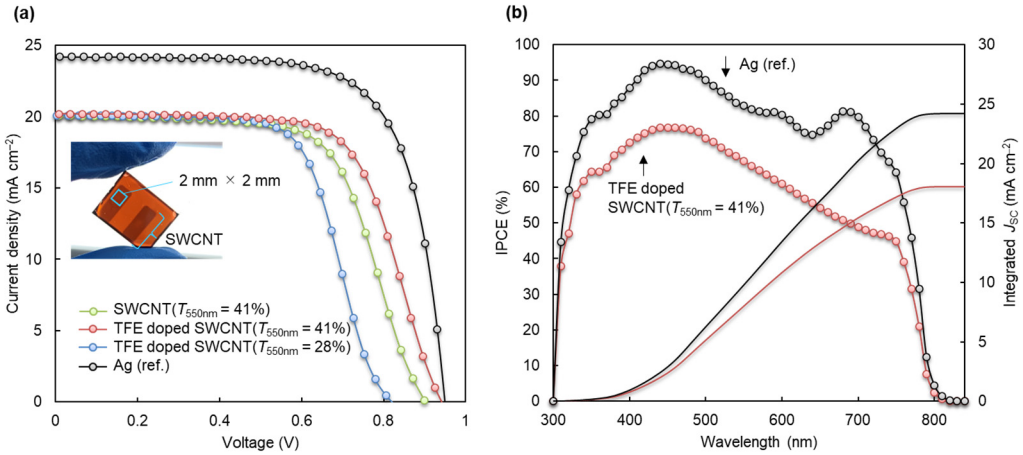

Figure 1. Effect of the TFE-doped SWCNT electrode on (**a**) *J*–*V* characteristics and (**b**) IPCE of the present perovskite solar cells. The solid line represents the integrated J_{SC}.

Table 1. Photovoltaic performance of the perovskite solar cells with SWCNTs.

Electrode	J_{SC} (mA cm^{-2})	V_{OC} (V)	FF	η (%)	R_S (Ω cm^2)	R_{Sh} (Ω cm^2)
SWCNT (T_{550nm} = 41%)	20.1	0.901	0.647	13.0	10.0	3446
TFE doped SWCNT (T_{550nm} = 41%)	20.2	0.941	0.670	14.1	10.3	5723
TFE doped SWCNT (T_{550nm} = 28%)	20.1	0.825	0.649	11.9	9.1	3980
Ag (ref.)	24.2	0.948	0.711	16.4	3.0	8041

As shown in Figure 2a, the cells with the TFE-doped SWCNT electrode exhibited a power-law dependence of J_{SC} on light intensity, described as $J_{SC} \propto P_{in}{}^{\alpha}$, where P_{in} is the light intensity and α is the power-law coefficient. The slopes of J_{SC} versus the logarithm of light intensity have the same values as the perovskite solar cells without TFE doping of SWCNTs, as shown in Table 2. The larger deviation of α from 1 means that the J_{SC} is limited by bimolecular recombination loss; thus, all cells exhibit weak bimolecular recombination loss [48–50]. Figure 2b shows the light intensity dependence of V_{OC}, described by $V_{OC} = \frac{mKT}{e}\ln\left(\frac{J_{SC}}{J_0}+1\right)$, where K is the Boltzmann constant, T is the temperature, and e is the elementary charge. J_{SC} refers to the short-circuit current density, while J_0 denotes the saturation current density. As light intensity increases, the number of photogenerated carriers rises, leading to an increase in J_{SC}. Consequently, with higher light intensity, V_{OC} also increases. J_0 depends on the quality of the material and its recombination characteristics. At lower light intensities, recombination processes decrease, and the number of photogenerated carriers decreases. This relatively amplifies the impact

of J_0, resulting in a tendency for V_{OC} to decrease. The slope is reduced from 3.92 to 2.55 for the TFE-doped SWCNT (T_{550nm} = 41%), indicating suppressed charge recombination. As shown in Figure 2c, the use of TFE drops lowers the carrier trap density, suggesting that TFE may help suppress carrier traps in the solar cell. Trap density (D_{trap}) can be calculated as $D_{trap} = \frac{2\varepsilon\varepsilon_0 V_{TFL}}{eL^2}$, where V_{TFL} is the trap-filled limit voltage, L is the thickness of the perovskite layer (500 nm), ε = 32 is the perovskite relative dielectric constant, and $\varepsilon_0 = 8.854 \times 10^{-14}$ F cm^{-1} is the vacuum permittivity [51,52]. This is interpreted as a factor contributing to the improved performance of the solar cell. Also, it was observed that devices without TFE have a smaller carrier trap density for SWCNT transmittance of T_{550nm} = 41% compared with T_{550nm} = 28%, as shown in Figure S4 and Table S2. It is hypothesized that more Spiro-OMeTAD solution permeates through the SWCNT electrode with T_{550nm} = 28% than through the one with T_{550nm} = 41% due to the greater film thickness for the lower transmittance. This increased Spiro-OMeTAD penetration may increase the resistance to carrier transfer. Increased film thickness tends to increase electron and hole transfer distances, thereby increasing carrier transport resistance.

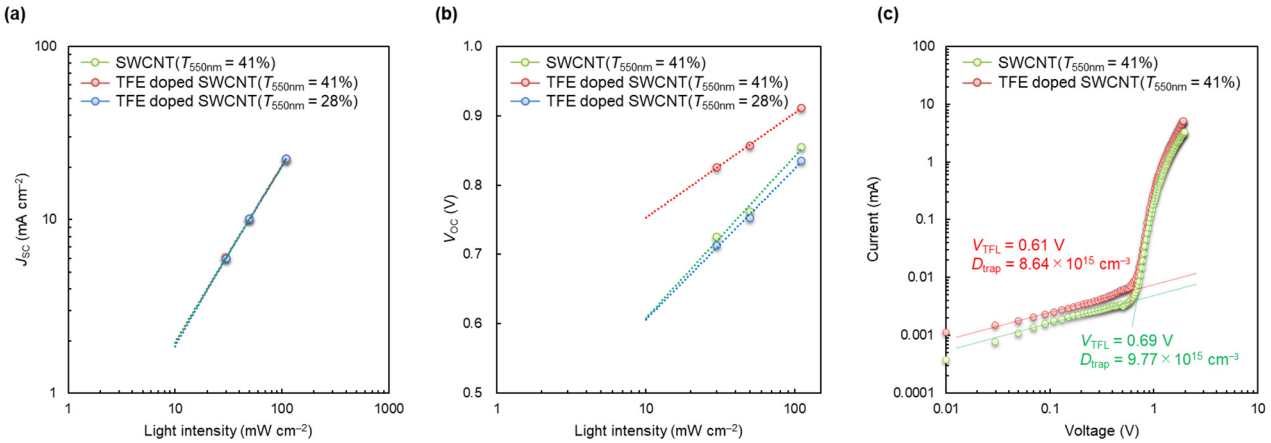

Figure 2. Light intensity dependence of *J*–*V* characteristics of (**a**) J_{SC} and (**b**) V_{OC} for devices with SWCNTs. (**c**) Dark current–voltage curves for the devices.

Table 2. Photovoltaic performance of the present devices.

Electrode	*m*	*α*
SWCNT (T_{550nm} = 41%)	3.95	1.01
TFE doped SWCNT (T_{550nm} = 41%)	2.55	1.01
TFE doped SWCNT (T_{550nm} = 28%)	3.68	1.03

Observing Figure 3 reveals that TFE doping results in a shift of aby 0.04 eV toward higher energy in the optical absorption peaks of SWCNTs. The perovskite layer primarily absorbs light within the wavelength range of 500 nm to 800 nm. In comparison, the SWCNTs absorb light primarily within the near-infrared range of 800 nm to 2400 nm. Perovskite solar cells can convert visible light within their absorption range into electrical energy. The inset shows that the band gap of $MAPbI_3$ is 1.55 eV. Optical absorption peaks were observed that originated from semiconducting and metallic SWCNTs. The metallic (E^M_{11}) and semiconducting (E^S_{22} and E^S_{11}) portions of SWCNTs have different optical properties, with the blue shift suggesting an increase in the band gap.

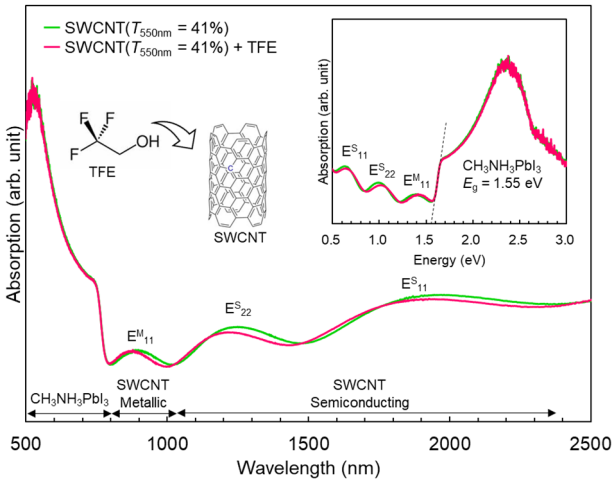

Figure 3. Optical absorption spectra of the present devices. The inset shows optical absorption with the axis of abscissa converted to energy.

As shown in Figure 4a, photoemission yield spectrometry showed a 0.04 eV decrease in the work function of TFE-doped SWCNTs, which is consistent with the shift in the optical absorption peak. Based on the energy diagram in Figure 4b, we can conclude that the barriers to carrier transport between Spiro-OMeTAD and CNT has been lowered, specifically the barrier to hole transport. Additionally, the sheet resistance of the SWCNTs with T_{550nm} = 41% decreased from 37.4 to 32.7 Ω/sq by doping with TFE (Table 3. The sheet resistance of SWCNT electrode with T_{550nm} = 28% and TFE doping was lower than that of the SWCNT electrode with T_{550nm} = 41% and TFE doping. Interestingly, however, the $\alpha\rho$ values were smaller for SWCNTs with lower transmittance. The parameter $\alpha\rho$ reflects SWCNT performance, with smaller values indicating improved SWCNT performance, and it is calculated as follows [53]:

$$\alpha\rho = -log\left(\frac{Transmittance(\%)}{100}\right) \times R_{Sheet} \quad (2)$$

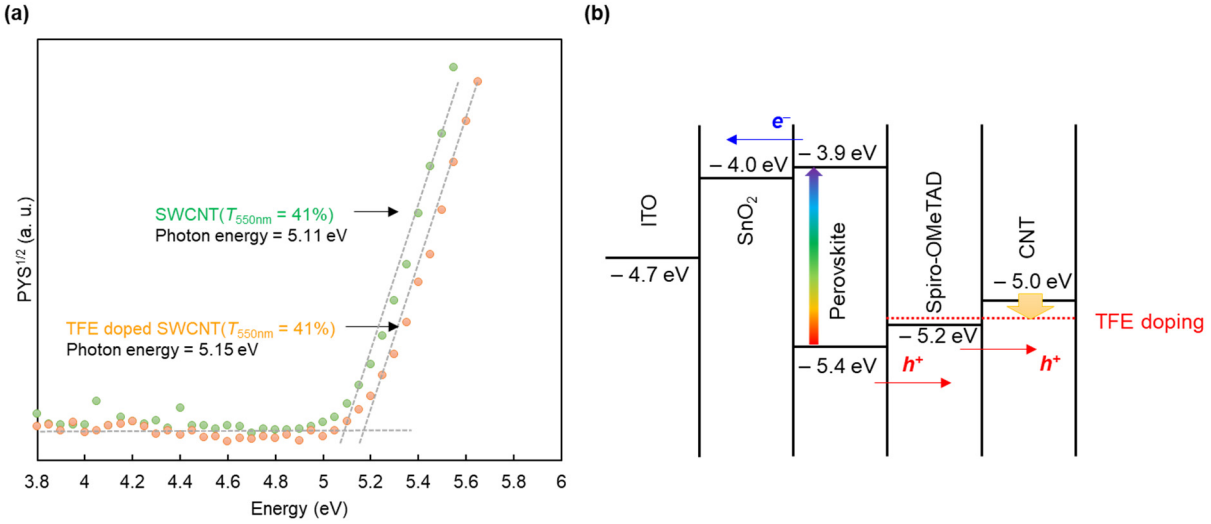

Figure 4. (**a**) Photoemission yield spectrometry data of SWCNTs doped with TFE. The suggested energy band diagrams are shown in (**b**).

Table 3. Sheet resistance of SWCNTs electrodes, along with calculated $\alpha\rho$ and conductivity parameters.

Electrode	R_{Sheet} (Ω/sq)	$\alpha\rho$	S/m
SWCNT (T_{550nm} = 41%)	37.4	14.9	6.5×10^4
TFE doped SWCNT (T_{550nm} = 41%)	32.7	12.7	7.4×10^4
TFE doped SWCNT (T_{550nm} = 28%)	23.9	13.2	1.3×10^5

This equation demonstrates that as the thickness of the SWCNT thin film increases, the transmittance decreases exponentially while the sheet resistance decreases inversely. Here, α represents absorbance and ρ represents resistivity. Therefore, changes in optical properties, such as the work function of the SWCNT surface due to TFE doping and the sheet resistance, can lead to more efficient hole transport.

No significant difference was observed in the SEM images of TFE-doped SWCNTs with T_{550nm} = 41% and T_{550nm} = 28%, which are shown in Figure 5a and Figure 5b, respectively. Interestingly, cross-sectional SEM observations of the SWCNT films revealed that the CNT film with T_{550nm} = 41% had a thickness of approximately 414 nm, while the SWCNT film with T_{550nm} = 28% had a thickness of approximately 317 nm, as shown in Figure 5c,d. Each layer was identified through elemental mapping, as shown in Figure S5. Unexpectedly, the SWCNT film with T_{550nm} = 28% was thinner. On the other hand, the SWCNT density in the T_{550nm} = 28% film was significantly higher, with individual SWCNTs being densely packed. Consequently, the conductivity of the SWCNT was calculated from the sheet resistance and film thickness, with the SWCNT with T_{550nm} = 28% showing the highest conductivity (Table 3). This result is also supported by the comparison of R_S values in Table 1, which shows that the SWCNT with T_{550nm} = 28% has a lower R_S than the SWCNT with T_{550nm} = 41%, indicating the validity of this outcome. Fe originating from the CNT growth catalysts was detected by energy-dispersive X-ray spectroscopy. It is not clear whether the performance degradation was due to Fe particles, and further investigation is needed regarding the dispersion state, as shown in Figure S3.

X-ray photoelectron spectroscopy (XPS) images shown in Figure 6a,c clearly demonstrate that the C–O peak was significantly smaller in glass/SWCNT/TFE, indicating the fewer hydrophilic groups and more hydrophobic surface of the SWCNT electrode. The C 1s peaks were fitted with five peaks: sp^2 (284.7 eV), sp^3 (285.1 eV), C–O (286.1 eV), C=O (288.9 eV), and π–π^* shake-up feature (291.0 eV) [54–56]. The 284.7 eV band is consistent with the literature on sp^2 hybridized carbon–carbon bonds found in CNTs, graphite, graphene, and reduced graphene oxide. The peak at 285.1 eV can be attributed to either sp^3 C–H bonds or graphite. Additionally, the C–O peak was significantly smaller in glass/SWCNT/TFE, indicating the fewer hydrophilic groups and more hydrophobic surface of the SWCNT electrode. As shown in Figure 6b,d, the O1s spectrum clearly indicates that the oxygen-containing groups present on the CNT surface are fewer in the glass/SWCNT/TFE sample. On the other hand, the C–F peak was detected in trace amounts after the TFE was applied. The sensitivity to humidity and low durability in perovskite solar cells has been a longstanding issue. For example, Spiro-OMeTAD, a commonly used hole transport material for ordinary perovskite structures, is considered sensitive to humidity. Specifically, the lithium salt dopant used in Spiro-OMeTAD has high hygroscopicity, which makes it susceptible to humidity, leading to degradation of the perovskite structure [57,58]. SWCNTs are hydrophobic and repel water. Additionally, they lack internal diffusion, like metal electrodes. This can improve the durability of perovskite solar cells. TFE was found to enhance hydrophobicity and reduce the impact of moisture on the perovskite solar cell surface, as shown by XPS measurements (Table 4).

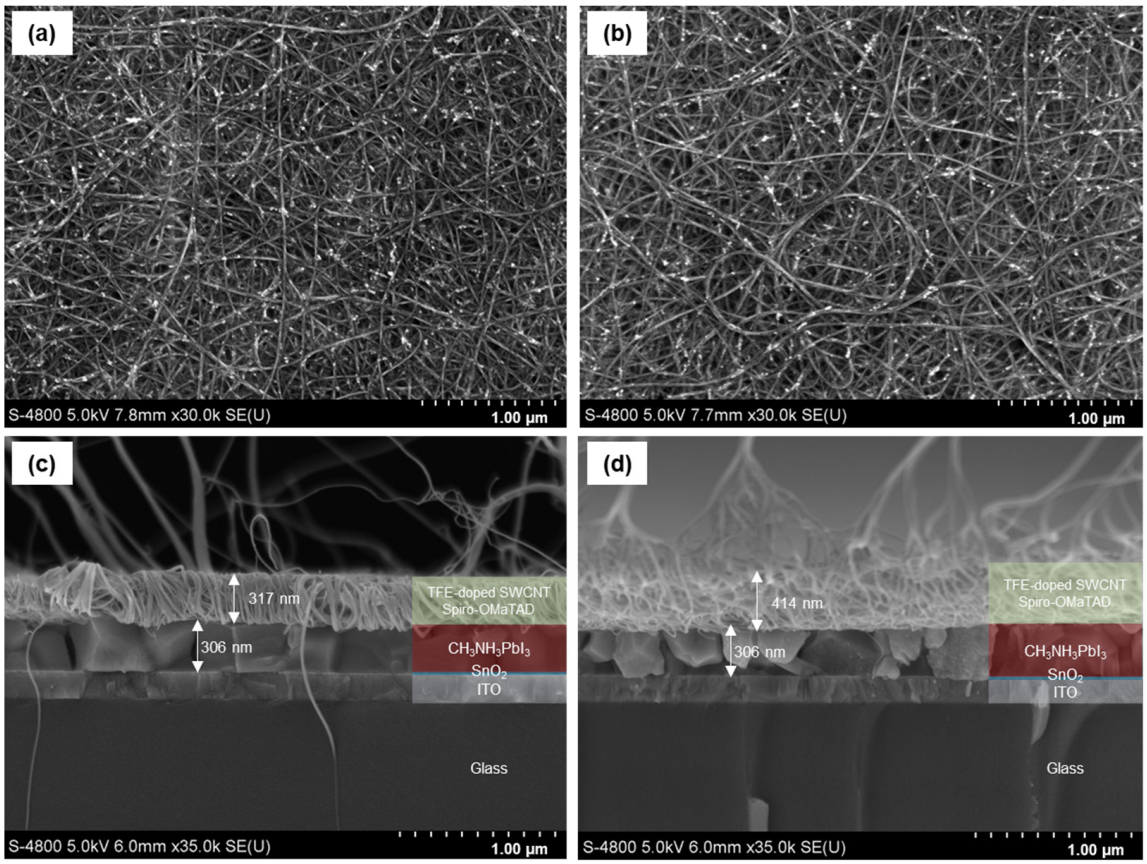

Figure 5. Surface SEM images of TFE-doped SWCNT with (**a**) T_{550nm} = 28% and (**b**) T_{550nm} = 41%. Cross-sectional SEM images of the perovskite solar cells with (**c**) SWCNT (T_{550nm} = 28%) and (**d**) SWCNT (T_{550nm} = 41%).

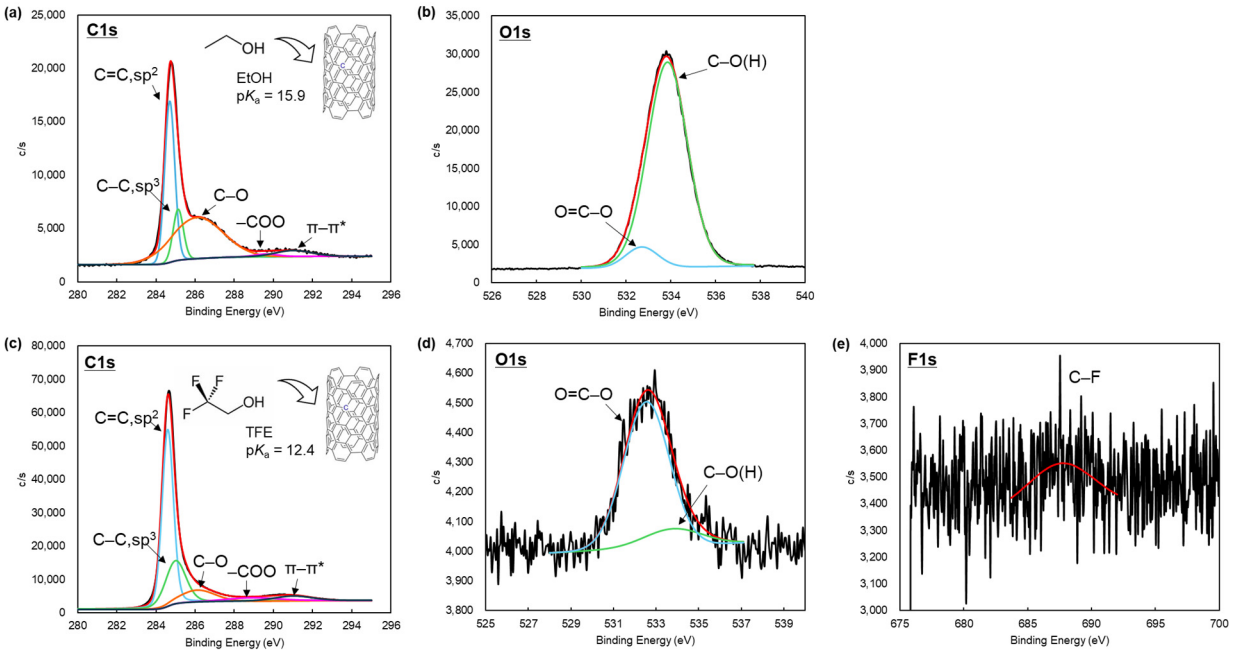

Figure 6. XPS spectra of C 1s, O1s, and F1s for pristine SWCNT and TFE-doped SWCNT. (**a**,**c**) show the C1s spectra of pristine SWCNT and TFE-doped SWCNT, respectively. (**b**,**d**) show the O1s spectra of pristine SWCNT and TFE-doped SWCNT, respectively. (**e**) shows the F1s spectra of TFE-doped SWCNT.

Table 4. Peak area ratio of each functional group of each sample eValuated by curve fitting.

Samples	C=C, sp^2 (%) (284.7 eV)	C–C, sp^3 (%) (285.1 eV)	C–O (%) (286.1 eV)	COO (%) (288.9 eV)	π-π* (%) (291.0 eV)
glass/SWCNT/EtOH	36	12	44	2	5
glass/SWCNT/TFE	61	17	12	6	4

The Raman spectral analysis found that the carbon nanotubes' G-band slightly shifted from 1593.6 cm^{-1} to 1592.1 cm^{-1} after the addition of TFE, as shown in Figure 7. This trend was consistently observed at three randomly selected points. This suggests that the TFE solution may act as a p-dopant, extracting electrons from the CNT, causing the G-band to shift to a lower frequency. On the other hand, the low-frequency signal is interpreted as the radial breathing mode (RBM). It is considered an important indicator for identifying the diameter and electronic properties of SWCNTs. The RBM appears primarily as a band consisting of multiple peaks, which is believed to result from the presence of multiple SWNTs with different diameters ranging from ~0.5 to 2 nm, corresponding to the frequency range of 100 to 300 cm^{-1}, according to the equation ω_{RBM} (cm^{-1}) = ~248/d (d is the diameter of the SWCNT) [59–61]. From the peak position with the highest intensity at 140 cm^{-1}, the diameter of the CNT was determined to be 1.76 nm.

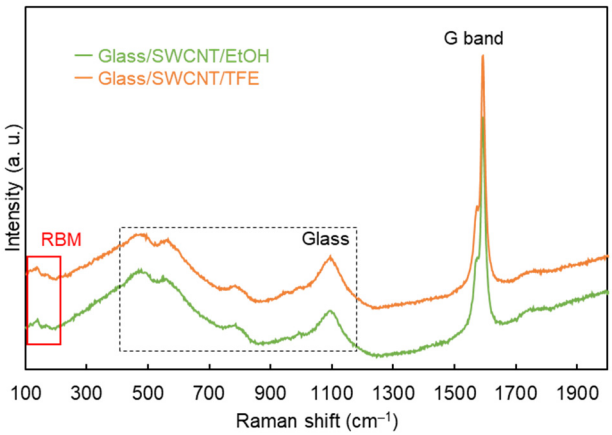

Figure 7. Raman spectra of the present SWCNT samples.

To measure the Seebeck coefficient of SWCNTs, we prepared a 15mm long SWCNT thin film transferred onto a glass substrate. We then dropped TFE and EtOH separately onto the film to prepare the samples. The Seebeck coefficients were measured to be 34.5 μV/K for EtOH and 73.1 μV/K for TFE at 40 °C, revealing an enhancement towards a more p-type semiconductor behavior. Thus, positive holes likely resulted in a decrease in electron density on the surface of the SWCNTs, leading to a reduction in charge recombination and a decrease in carrier trap density, as shown in Table 2.

XRD data showed the stability of perovskite crystals stored under atmospheric conditions (Figure 8a). The perovskite structure investigated here was found to be tetragonal [62]. Usually, $MAPbI_3$ has a tetragonal structure at room temperature. However, when substances such as HI and CH_3NH_2 are released from the perovskite crystal, the structure transforms into PbI_2 crystals [63]. A comparison of cells over 30 days suggested that the formation of PbI_2 is suppressed when drops of TFE are applied (red arrow). This indicates that the use of TFE improved the durability of the perovskite structure; it was noted earlier that TFE provides hydrophobicity, which may have the effect of reducing the effects of external factors such as humidity, making the perovskite structure more stable. In a stability eValuation, the conversion efficiency decreased by 57% from the initial efficiency after 30 days for SWCNTs with T_{550nm} = 41% but by 34% for SWCNTs with T_{550nm} = 41% and TFE doping, as shown in Figure 8b. It is worth mentioning that SWCNTs with T_{550nm} = 28% exhibited the smallest decrease, by 24%. The permeability decreased with increasing film

thickness; thus, the potential for TFE to penetrate and remain in the SWCNT thin film increased. This TFE residue would have contributed to the improved stability of the conversion efficiency. The boiling point of TFE is 73.6 °C, so it may gradually volatilize from the SWCNT surface due to thermal effects. Considering this property, TFE was applied to the cell again after 30 days, and the conversion efficiency was investigated (Figure S7a and Table S3). The FF increased slightly, and the conversion efficiency improved by 1%. The re-addition of TFE probably allowed TFE to penetrate the SWCNT thin film, enhancing its surface hydrophobicity and stability. Furthermore, Figure S7b indicates that the effect might persist eVen after 260 days. When TFE was reapplied, a slight increase in conversion efficiency was observed. Figure S7c clearly shows that the perovskite crystals around the Ag electrode have turned yellow and degraded, whereas the SWCNT electrode effectively inhibited this degradation. To verify the hydrophobicity of the SWCNT surface treated with TFE, three samples were prepared: glass/SWCNT/EtOH, glass/SWCNT/spiro-OMeTAD, and glass/SWCNT/spiro-OMeTAD/TFE. As shown in Figure S8, the contact angle significantly decreased for Spiro-OMeTAD, indicating sufficient water absorption. Upon the application of TFE, the contact angle slightly increased from 63.1 degrees to 67.9 degrees, indicating a slight hydrophobic effect, suggesting the potential to maintain the original hydrophobicity of the SWCNT. Similarly, as eVidenced by the XPS results, TFE likely removed impurities from the SWCNT surface and acted as a surface-protective layer, preventing oxygen penetration. Suppose TFE remains at the interface between the perovskite crystals and the SWCNT. In that case, its fluoroalkyl groups may form hydrogen bonds with the molecules of SWCNT and $MAPbI_3$, potentially enhancing interface stability. Consequently, this might have inhibited the degradation of the perovskite crystals [64,65]. A comparison table with previous studies employing SWCNTs is shown in Table S4. As this study uses $CH_3NH_3PbI_3$, it is expected that the conversion efficiency could be further improved by incorporating formamidinium or bromine.

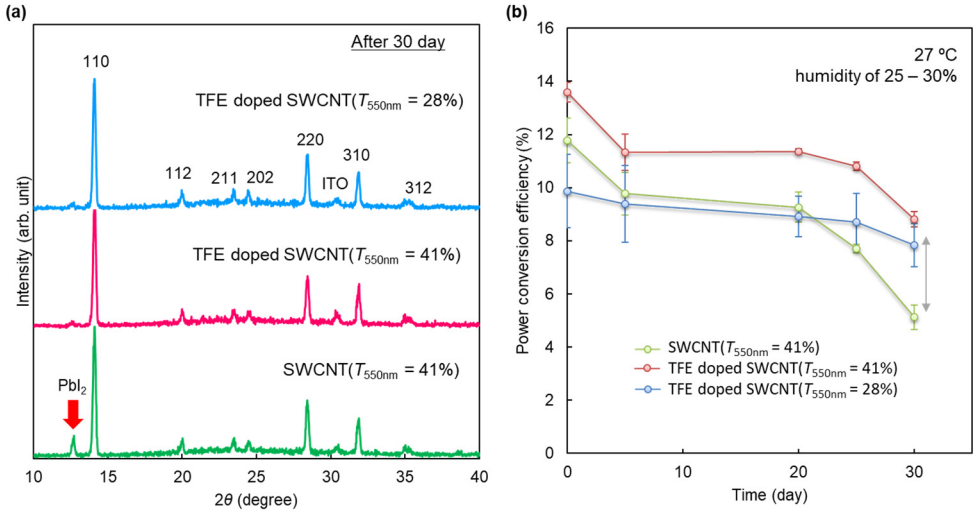

Figure 8. Stability data for the device. (**a**) XRD patterns after 30 days and (**b**) changes in conversion efficiency of the present perovskite solar cells.

4. Conclusions

The study examined the impact of adding TFE as a dopant in perovskite solar cells when using SWCNTs instead of traditional metal electrodes. TFE was applied to the SWCNT electrodes, resulting in a power conversion efficiency of 14.1% using a SWCNT film electrode with transmittance of 41%. By comparing perovskite solar cells using SWCNTs with transmittances of 41% and 28%, it was revealed that the conversion efficiency is superior when employing a transmittance of 41%. At the interface between Spiro-OMeTAD and SWCNT, the ionization potential of the SWCNT thin film was shown to shift to a slightly deeper level, which reduced the barrier to carrier transport. The Seebeck coefficient

indicated that after the deposition of TFE, the surface of SWCNTs became enriched with positive holes, resulting in a slight reduction in carrier trap density and an improvement in conductivity of the SWCNTs. Because of hydrophobicity of TFE, the decomposition of the perovskite crystals was inhibited over 260 days, contributing to stability. Although the boiling point of TFE was lower than that of TFMS, the doping effect was kept at least for 260 days. A significant advantage was that TFE can be doped directly onto SWCNT electrodes without concentration adjustment without damaging the perovskite crystals, and it is safe due to its low acidity. Therefore, TFE could serve as a p-dopant for SWCNT top electrodes in advancing perovskite solar cells.

Supplementary Materials: The following supporting information can be downloaded at: https://www.mdpi.com/article/10.3390/photochem4030019/s1, Figure S1: *J–V* characteristics of the present perovskite solar cells; Figure S2: Device performance. (a)–(f) Statistics deviation of the photovoltaic parameters of the perovskite solar cells with TFE-doped CNT. The statistical data was collected from five cells; Figure S3: (a) IQE spectra calculated by EQE results and light absorption efficiency. (b) Transmittance spectra of the perovskite solar cells; Figure S4: Light intensity dependence of *J–V* characteristics of (a) V_{OC} and (b) J_{SC} for devices with SWCNTs. (c) Dark current–voltage curves for the devices without TFE; Figure S5: Elemental mapping images of In L, Sn L, Si K, C L, N K, I L, and Pb M lines; Figure S6: SEM image and EDX data of the SWCNT (T_{550nm} = 41%) film; Figure S7: Time-dependent eValuation. *J–V* characteristics of the cells after (a) after 30 days and (b) after 260 days. (c) Photograph of the backside of the present perovskite solar cells after 260 days; Table S1: Photovoltaic performance of the cells with SWCNTs; Table S2: Photovoltaic performance of the cells with SWCNTs non-doped TFE; Table S3: Photovoltaic performance of the cells with SWCNTs after 30 days and 260 days; Table S4 Comparison of carbon nanotubes as hole transport materials in perovskite solar cells [66–75].

Author Contributions: All authors conceived and designed the study. N.U. and A.S.H. performed the experiments. N.U. and Y.M. analyzed the data. H.O. and Y.H. contributed SWCNT films. N.U. and Y.M. wrote the paper. All authors have read and agreed to the published version of the manuscript.

Funding: This work was financially supported by the Japan Society for the Promotion of Science (JSPS) KAKENHI (Grant Numbers 21KK0087 and 23H05443) and the DENSO CORPORATION. This work was also financially supported by JST SPRING, Grant Number JPMJSP2125.

Data Availability Statement: Data are contained within the article.

Acknowledgments: Y.M. thanks the Takahashi Industrial and Economic Research Foundation and the Yashima Environment Technology Foundation for financial support. The authors would like to appreciate the collaboration of Hieda Junko and Zai Yongchang from Nagoya University for the water contact angle measurements.

Conflicts of Interest: The authors declare no conflicts of interest. Author Yoshimasa Hijikata was employed by the company DENSO CORPORATION. The remaining authors declare that the research was conducted in the absence of any commercial or financial relationships that could be construed as a potential conflict of interest.

References

1. Kojima, A.; Teshima, K.; Shirai, Y.; Miyasaka, T. Organometal halide perovskites as visible-light sensitizers for photovoltaic cells. *J. Am. Chem. Soc.* **2009**, *131*, 6050–6051. [CrossRef] [PubMed]
2. Li, X.; Bi, D.; Yi, C.; Décoppet, J.-D.; Luo, J.; Zakeeruddin, S.M.; Hagfeldt, A.; Grätzel, M. A vacuum flash–assisted solution process for high-efficiency large-area perovskite solar cells. *Science* **2016**, *353*, 58–62. [CrossRef] [PubMed]
3. Zhong, J.-X.; Wu, W.-Q.; Zhou, Y.; Dong, Q.; Wang, P.; Ma, H.; Wang, Z.; Yao, C.-Y.; Chen, X.; Liu, G.-l.; et al. Room Temperature Fabrication of SnO_2 Electrodes Enabling Barrier-Free Electron Extraction for Efficient Flexible Perovskite Photovoltaics. *Adv. Funct. Mater.* **2022**, *32*, 2200817. [CrossRef]
4. Meng, Y.; Li, X.; Wang, S.; Lau, C.; Hu, H.; Ke, Y.; Tan, G.; Yang, J.; Long, Y. Flexible smart photovoltaic foil for energy generation and conservation in buildings. *Nano Energy* **2022**, *91*, 106632. [CrossRef]
5. Nukunudompanich, M.; Sriprapai, D.; Sontikaew, S. Aspects of optical and thermal performances in flexible perovskite solar cells made of nanomaterials with potential for development of vehicle-integrated photovoltaics. *Mater. Today Proc.* **2022**, *66*, 3163–3167. [CrossRef]

6. Koh, T.M.; Wang, H.; Ng, Y.F.; Bruno, A.; Mhaisalkar, S.; Mathews, N. Halide Perovskite Solar Cells for Building Integrated Photovoltaics: Transforming Building Façades into Power Generators. *Adv. Mater.* **2022**, *34*, 2104661. [CrossRef]
7. Li, M.; Wang, Z.-K.; Zhuo, M.-P.; Hu, Y.; Hu, K.-H.; Ye, Q.-Q.; Jain, S.M.; Yang, Y.-G.; Gao, X.-Y.; Liao, L.-S. Pb–Sn–Cu Ternary Organometallic Halide Perovskite Solar Cells. *Adv. Mater.* **2018**, *30*, 1800258. [CrossRef] [PubMed]
8. Wang, Y.; Li, W.; Yin, Y.; Wang, M.; Cai, W.; Shi, Y.; Guo, J.; Shang, W.; Zhang, C.; Dong, Q.; et al. Defective MWCNT Enabled Dual Interface Coupling for Carbon-Based Perovskite Solar Cells with Efficiency Exceeding 22%. *Adv. Funct. Mater.* **2022**, *32*, 2204831. [CrossRef]
9. Wang, C.; Zhu, Z.; Wang, G.; Ding, X.; Chen, Y.; Xiao, S.; Liu, X.; Zhang, X.; Wen, S. Crystallization and Defect Chemistry Dual Engineering for $MAPbI_3$ Perovskite Solar Cells with Efficiency Approaching 22%. *ACS Sustain. Chem. Eng.* **2022**, *10*, 17318–17326. [CrossRef]
10. Yin, W.J.; Shi, T.; Yan, Y. Unusual defect physics in $CH_3NH_3PbI_3$ perovskite solar cell absorber. *Appl. Phys. Lett.* **2014**, *104*, 063903. [CrossRef]
11. Yin, W.-J.; Shi, T.; Yan, Y. Unique Properties of Halide Perovskites as Possible Origins of the Superior Solar Cell Performance. *Adv. Mater.* **2014**, *26*, 4653–4658.
12. Zhao, Y.; Zhu, K. Efficient Planar Perovskite Solar Cells Based on 1.8 eV Band Gap $CH_3NH_3PbI_2Br$ Nanosheets via Thermal Decomposition. *J. Am. Chem. Soc.* **2014**, *136*, 12241–12244. [CrossRef]
13. Jung, Y.-S.; Hwang, K.; Heo, Y.-J.; Kim, J.-E.; Vak, D.; Kim, D.-Y. Progress in Scalable Coating and Roll-to-Roll Compatible Printing Processes of Perovskite Solar Cells toward Realization of Commercialization. *Adv. Opt. Mater.* **2018**, *6*, 1701182. [CrossRef]
14. GuO, Z.; Jena, A.K.; Kim, G.M.; Miyasaka, T. The high open-circuit voltage of perovskite solar cells: A review. *Energy Environ. Sci.* **2022**, *15*, 3171–3222. [CrossRef]
15. Li, L.; Zhang, R.; Wu, Z.; Wang, Y.; Hong, J.; Rao, H.; Pan, Z.; Zhong, X. Crystallization control of air-processed wide-bandgap perovskite for carbon-based perovskite solar cells with 17.69% efficiency. *Chem. Eng. J.* **2023**, *455*, 140566. [CrossRef]
16. Lee, H.; Lee, C. Analysis of Ion-Diffusion-Induced Interface Degradation in Inverted Perovskite Solar Cells via Restoration of the Ag Electrode. *Adv. Energy Mater.* **2018**, *8*, 1702197. [CrossRef]
17. Zhao, J.; Zheng, X.; Deng, Y.; Li, T.; Shao, Y.; Gruverman, A.; Shield, J.; Huang, J. Is Cu a stable electrode material in hybrid perovskite solar cells for a 30-year lifetime? *Energy Environ. Sci.* **2016**, *9*, 3650–3656. [CrossRef]
18. Ueoka, N.; Oku, T. Additive effects of alkali metals on Cu-modified $CH_3NH_3PbI_{3-\delta}Cl_\delta$ photovoltaic devices. *RSC Adv.* **2019**, *9*, 24231–24240. [CrossRef]
19. Huijie, T.; Cao, Q.; He, Z.; Wang, S.; Han, J.; Li, T.; Gao, B.; Yang, J.; Deng, D.; Li, X. SnO_2–Carbon Nanotubes Hybrid Electron Transport Layer for Efficient and Hysteresis-Free Planar Perovskite Solar Cells. *Sol. RRL* **2020**, *4*, 1900415.
20. Ming, W.; Yang, D.; Li, T.; Zhang, L.; Du, M.-H. Formation and Diffusion of Metal Impurities in Perovskite Solar Cell Material $CH_3NH_3PbI_3$: Implications on Solar Cell Degradation and Choice of Electrode. *Adv. Sci.* **2018**, *5*, 1700662. [CrossRef]
21. Baydin, A.; Tay, F.; Fan, J.; Manjappa, M.; Gao, W.; Kono, J. Carbon Nanotube Devices for Quantum Technology. *Materials* **2022**, *15*, 1535. [CrossRef] [PubMed]
22. Liu, S.; Li, H.; He, C. Simultaneous enhancement of electrical conductivity and seebeck coefficient in organic thermoelectric SWNT/PEDOT:PSS nanocomposites. *Carbon* **2019**, *149*, 25–32. [CrossRef]
23. Hata, S.; Shiraishi, M.; Yasuda, S.; Juhasz, G.; Du, Y.; Shiraishi, Y.; Toshima, N. Green Route for Fabrication of Water-Treatable Thermoelectric Generators. *Energy Mater. Adv.* **2022**, *2022*, 9854657. [CrossRef]
24. Nonoguchi, Y.; Ohashi, K.; Kanazawa, R.; Ashiba, K.; Hata, K.; Nakagawa, T.; Adachi, C.; Tanase, T.; Kawai, T. Systematic Conversion of Single Walled Carbon Nanotubes into n-type Thermoelectric Materials by Molecular Dopants. *Sci. Rep.* **2013**, *3*, 3344. [CrossRef] [PubMed]
25. Shin, D.-W.; Lee, J.H.; Kim, Y.-H.; Yu, S.M.; Park, S.-Y.; Yoo, J.-B. A role of HNO_3 on transparent conducting film with single-walled carbon nanotubes. *Nanotechnology* **2009**, *20*, 475703. [CrossRef] [PubMed]
26. Jeon, I.; Seo, S.; Sato, Y.; Delacou, C.; Anisimov, A.; Suenaga, K.; Kauppinen, E.I.; Maruyama, S.; Matsuo, Y. Perovskite Solar Cells Using Carbon Nanotubes Both as Cathode and as Anode. *J. Phys. Chem. C* **2017**, *121*, 25743–25749. [CrossRef]
27. Lee, J.-W.; Jeon, I.; Lin, H.-S.; Seo, S.; Han, T.-H.; Anisimov, A.; Kauppinen, E.I.; Matsuo, Y.; Maruyama, S.; Yang, Y. Vapor-Assisted Ex-Situ Doping of Carbon Nanotube toward Efficient and Stable Perovskite Solar Cells. *Nano Lett.* **2019**, *19*, 2223–2230. [CrossRef] [PubMed]
28. Aharon, S.; Dymshits, A.; Rotem, A.; Etgar, L. Temperature dependence of hole conductor free formamidinium lead iodide perovskite based solar cells. *J. Mater. Chem. A* **2015**, *3*, 9171–9178. [CrossRef]
29. Choi, H.; Jeong, J.; Kim, H.-B.; Kim, S.; Walker, B.; Kim, G.-H.; Kim, J.Y. Cesium-doped methylammonium lead iodide perovskite light absorber for hybrid solar cells. *Nano Energy* **2014**, *7*, 80–85. [CrossRef]
30. Ueoka, N.; Oku, T.; Suzuki, A. Effects of doping with Na, K, Rb, and formamidinium cations on $(CH_3NH_3)_{0.99}Rb_{0.01}Pb_{0.99}Cu_{0.01}I_{3-x}(Cl, Br)_x$ perovskite photovoltaic cells. *AIP Adv.* **2020**, *10*, 125023. [CrossRef]
31. Jeon, I.; Cui, K.; Chiba, T.; Anisimov, A.; Nasibulin, A.G.; Kauppinen, E.I.; Maruyama, S.; Matsuo, Y. Direct and Dry Deposited Single-Walled Carbon Nanotube Films Doped with MoO_x as Electron-Blocking Transparent Electrodes for Flexible Organic Solar Cells. *J. Am. Chem. Soc.* **2015**, *137*, 7982–7985. [CrossRef] [PubMed]

32. Jeon, I.; Yoon, J.; Ahn, N.; Atwa, M.; Delacou, C.; Anisimov, A.; Kauppinen, E.I.; Choi, M.; Maruyama, S.; Matsuo, Y. Carbon Nanotubes versus Graphene as Flexible Transparent Electrodes in Inverted Perovskite Solar Cells. *J. Phys. Chem. Lett.* **2017**, *8*, 5395–5401. [CrossRef] [PubMed]
33. Matsuo, Y. Creation of Highly Efficient and Durable Organic and Perovskite Solar Cells Using Nanocarbon Materials. *Bull. Chem. Soc. Jpn.* **2021**, *94*, 1080–1089. [CrossRef]
34. Jeon, I.; Delacou, C.; Okada, H.; Morse, G.E.; Han, T.-H.; Sato, Y.; Anisimov, A.; Suenaga, K.; Kauppinen, E.I.; Maruyama, S.; et al. Polymeric acid-doped transparent carbon nanotube electrodes for organic solar cells with the longest doping durability. *J. Mater. Chem. A* **2018**, *6*, 14553–14559. [CrossRef]
35. Gente, G.; Mesa, C.L. Water–Trifluoroethanol Mixtures: Some Physicochemical Properties. *J. Solution. Chem.* **2000**, *29*, 1159–1172. [CrossRef]
36. Moisala, A.; Nasibulin, A.G.; Brown, D.P.; Jiang, H.; Khriachtchev, L.; Kauppinen, E.I. Single-walled carbon nanotube synthesis using ferrocene and iron pentacarbonyl in a laminar flow reactor. *Chem. Eng. Sci.* **2006**, *61*, 4393–4402. [CrossRef]
37. Kaskela, A.; Nasibulin, A.G.; Timmermans, M.Y.; Aitchison, B.; Papadimitratos, A.; Tian, Y.; Zhu, Z.; Jiang, H.; Brown, D.P.; Zakhidov, A.; et al. Aerosol-Synthesized SWCNT Networks with Tunable Conductivity and Transparency by a Dry Transfer Technique. *Nano Lett.* **2010**, *10*, 4349–4355. [CrossRef]
38. Oshima, H.; Iwase, K.; Ohno, Y. In situ monitoring of the electrical property of carbon nanotube thin film in floating catalyst chemical vapor deposition. *Jpn. Appl. Phys.* **2022**, *61*, 038002. [CrossRef]
39. Matsuo, Y.; Ishikawa, S.; Amada, H.; Yokoyama, K.; Shui, Q.-J.; Huda, M.; Ueoka, N.; Lin, H.-S. eVaporable Indano[60]fullerene Ketone for the Electron Transport Layer of Inverted Perovskite Solar Cells. *Chem. Lett.* **2023**, *52*, 685–687. [CrossRef]
40. Ma, D.; Lin, K.; Dong, Y.; Choubisa, H.; Proppe, A.H.; Wu, D.; Wang, Y.K.; Chen, B.; Li, P.; Fan, J.Z.; et al. Distribution control enables efficient reduced-dimensional perovskite LED. *Nature* **2021**, *599*, 594–598. [CrossRef]
41. Richter, M.; Hammer, M.; Sonnet, T.; Parisi, J. Bandgap extraction from quantum efficiency spectra of Cu(In,Ga)Se_2 solar cells with varied grading profile and diffusion length. *Thin Solid Film.* **2017**, *633*, 213–217. [CrossRef]
42. Nasir, A.; Ahmad, S.; Khan, M.; Bragazzi, N.L. Resent Advancement on Crystalline quality, IQE, and EQE of III-nitride-based deep-ultraviolet light-emitting diodes: Comprehensive Review. Available online: https://ssrn.com/abstract=3842127 (accessed on 1 May 2021).
43. Nakka, L.; Cheng, Y.; Aberle, A.G.; Lin, F. Analytical Review of Spiro-OMeTAD Hole Transport Materials: Paths Toward Stable and Efficient Perovskite Solar Cells. *Adv. Energy Sustain. Res.* **2022**, *3*, 2200045. [CrossRef]
44. Makuta, S.; Liu, M.; Endo, M.; Nishimura, H.; Wakamiya, A.; Tachibana, Y. Photo-excitation intensity dependent electron and hole injections from lead iodide perovskite to nanocrystalline TiO_2 and spiro-OMeTAD. *Chem. Commun.* **2016**, *52*, 673–676. [CrossRef] [PubMed]
45. Li, R.; Liu, M.; Matta, S.K.; Hiltunen, A.; Deng, Z.; Wang, C.; Dai, Z.; Russo, S.P.; Vivo, P.; Zhang, H. Sulfonated Dopant-Free Hole-Transport Material Promotes Interfacial Charge Transfer Dynamics for Highly Stable Perovskite Solar Cells. *Adv. Sustainable Syst.* **2021**, *5*, 2100244. [CrossRef]
46. Brauer, J.C.; Lee, Y.H.; Nazeeruddin, M.K.; Baneji, N. Ultrafast charge carrier dynamics in $CH_3NH_3PbI_3$:evidence for hot hole injection into spiro-OMeTAD. *J. Mater. Chem. C* **2016**, *4*, 5922–5931. [CrossRef]
47. Abdelraouf, O.A.M.; Allam, N.K. Towards nanostructured perovskite solar cells with enhanced efficiency: Coupled optical and electrical modeling. *Sol. Energy* **2016**, *137*, 364–370. [CrossRef]
48. Zhu, T.; Yang, Y.; Yao, X.; Huang, Z.; Liu, L.; Hu, W.; Gong, X. Solution-Processed Polymeric Thin Film as the Transparent Electrode for Flexible Perovskite Solar Cells. *ACS Appl. Mater. Interfaces* **2020**, *12*, 15456–15463. [CrossRef] [PubMed]
49. Jianga, T.; Fu, W. Improved performance and stability of perovskite solar cells with bilayer electron-transporting layers. *RSC Adv.* **2018**, *8*, 5897–5901. [CrossRef]
50. Kyaw, A.K.K.; Wang, D.H.; Wynands, D.; Zhang, J.; Nguyen, T.-Q.; Bazan, G.C.; Heeger, A.J. Improved Light Harvesting and Improved Efficiency by Insertion of an Optical Spacer (ZnO) in Solution-Processed Small-Molecule Solar Cells. *Nano Lett.* **2013**, *13*, 3796–3801. [CrossRef]
51. Singh, R.; Sandhu, S.; Yadav, H.; Lee, J.-J. Stable Triple-Cation (Cs^+–MA^+–FA^+) Perovskite Powder Formation under Ambient Conditions for Hysteresis-Free High-Efficiency Solar Cells. *ACS Appl. Mater. Interfaces* **2019**, *11*, 29941–29949. [CrossRef]
52. Hua, W.; Niu, Q.; Zhang, L.; Chai, B.; Yang, J.; Zeng, W.; Xia, R.; Min, Y. Enhancing the Performance of Perovskite Solar Cells by Introducing 4-(Trifluoromethyl)-1H-imidazole Passivation Agents. *Molecules* **2023**, *28*, 4976. [CrossRef] [PubMed]
53. Fukaya, N.; Kim, D.Y.; Kishimoto, S.; Noda, S.; Ohno, Y. One-Step Sub-10 μm Patterning of Carbon-Nanotube Thin Films for Transparent Conductor Applications. *ACS Nano* **2014**, *8*, 3285. [CrossRef] [PubMed]
54. Cheng, I.F.; Xie, Y.; Gonzales, R.A.; Brejna, P.R.; Sundararajan, J.P.; Kengne, B.A.F.; Aston, D.E.; McIlroy, D.N.; Foutch, J.D.; Griffiths, P.R. Synthesis of graphene paper from pyrolyzed asphalt. *Carbon* **2011**, *49*, 2852–2861. [CrossRef]
55. Youn, H.-C.; Bak, S.-M.; Park, S.-H.; Yoon, S.-B.; Roh, K.C.; Kim, K.-B. One-step preparation of reduced graphene oxide/carbon nanotube hybrid thin film by electrostatic spray deposition for supercapacitor applications. *Met. Mater. Int.* **2014**, *20*, 975–981. [CrossRef]
56. Varga, M.; Izak, T.; Vretenar, V.; Kozak, H.; Holovsky, J.; Artemenko, A.; Hulman, M.; Skakalova, V.; Lee, D.S.; Kromka, A. Diamond/carbon nanotube composites: Raman, FTIR and XPS spectroscopic studies. *Carbon* **2017**, *111*, 54–61. [CrossRef]

57. Ulzii, G.T.; Matsushima, T.; Adachi, C. Mini-Review on Efficiency and Stability of Perovskite Solar Cells with Spiro-OMeTAD Hole Transport Layer: Recent Progress and Perspectives. *Energy Fuels* **2021**, *35*, 18915–18927. [CrossRef]
58. Jeon, I.; Ueno, H.; Seo, S.; Kerttu, A.; Nishikubo, R.; Saeki, A.; Okada, H.; Boschloo, G.; Shigeo, M.; Matsuo, Y. Lithium-Ion Endohedral Fullerene (Li+@C60) Dopants in Stable Perovskite Solar Cells Induce Instant Doping and Anti-Oxidation. *Angew. Chem. Int. Ed.* **2018**, *57*, 4607–4611. [CrossRef] [PubMed]
59. Kumar, A.Y.; Singh, P. A review of the structures of oxide glasses by Raman spectroscopy. *RSC Adv.* **2015**, *5*, 67583–67609.
60. Marković, Z.; Kepić, D.; Antunović, I.H.; Nikolić, M.; Dramićanin, M.; Cincović, M.D.; Marković, B.T. Raman study of single wall carbon nanotube thin films treated by laser irradiation and dynamic and isothermal oxidation. *J. Raman Spectrosc.* **2012**, *43*, 1413–1422. [CrossRef]
61. Hembram, K.P.S.S.; Kim, J.G.; Lee, S.G.; Park, J.; Lee, J.K. Radial-tangential made of single-wall carbon nanotubes manifested by Landau regulation: Reinterpretation of low-and intermediate-frequency Raman signals. *Sci. Rep.* **2023**, *13*, 5012. [CrossRef]
62. Oku, T. Crystal Structures of $CH_3NH_3PbI_3$ and Related Perovskite Compounds Used for Solar cells. In *Solar Cells-New Approaches and Reviews*; IntechOpen: London, UK, 2015.
63. Ueoka, N.; Oku, T. Stability Characterization of PbI_2-Added $CH_3NH_3PbI_{3-x}Cl_x$ Photovoltaic Devices. *ACS Appl. Mater. Interfaces* **2018**, *10*, 44443–44451. [CrossRef] [PubMed]
64. Zhu, C.; Wang, C.; Zhang, P.; Ma, S.; Chen, Y.; Zhang, Y.; Yang, N.; Xiao, M.; Cheng, X.; Gao, Z.; et al. Topochemical assembly minimizes lattice heterogeneity in polycrystalline halide perovskites. *Joule* **2023**, *7*, 2361–2375. [CrossRef]
65. Zhu, C.; Wang, X.; Li, H.; Wang, C.; Gao, Z.; Zhang, P.; Niu, X.; Li, N.; Xu, Z.; Su, Z.; et al. Stress compensation based on interfacial nanostructures for stable perovskite solar cells. *Interdiscip. Mater.* **2023**, *2*, 348–359. [CrossRef]
66. Li, Z.; Boix, P.P.; Xing, G.; Fu, K.; Kulkarni, S.K.; Xu, W.; Cao, A.; Sum, T.C.; Mathews, N.; Wong, L.H. Carbon nanotubes as an efficient hole collector for high voltage methylammonium lead bromide perovskite solar cells. *Nanoscale* **2016**, *8*, 6352–6360. [CrossRef] [PubMed]
67. Habisreutinger, S.N.; Leijtens, T.; Eperon, G.E.; Stranks, S.D.; Nicholas, R.J.; Snaith, H.J. Carbon Nanotube/Polymer Composites as a Highly Stable Hole Collection Layer in Perovskite Solar Cells. *Nano Lett.* **2014**, *14*, 5561–5568. [CrossRef] [PubMed]
68. Wang, F.; Endo, M.; Mouri, S.; Miyauchi, Y.; Ohno, Y.; Wakamiya, A.; Murata, Y.; Matsuda, K. Highly stable perovskite solar cells with an all-carbon hole transport layer. *Nanoscale* **2016**, *8*, 11882–11888. [CrossRef] [PubMed]
69. Habisreutinger, S.N.; Leijtens, T.; Eperon, G.E.; Stranks, S.D.; Nicholas, R.J.; Snait, H.J. Enhanced Hole Extraction in Perovskite Solar Cells Through Carbon Nanotubes. *J. Phys. Chem. Lett.* **2014**, *5*, 4207–4212. [CrossRef] [PubMed]
70. Habisreutinger, S.N.; Wenger, B.; Snaith, H.J.; Nicholas, R.J. Dopant-Free Planar n–i–p Perovskite Solar Cells with Steady-State Efficiencies Exceeding 18%. *ACS Energy Lett.* **2017**, *2*, 622–628. [CrossRef]
71. Mazzotta, G.; Dollmann, M.; Habisreutinger, S.N.; Christoforo, M.G.; Wang, Z.; Snaith, H.J.; Riede, M.K.; Nicholas, R.J. Solubilization of Carbon Nanotubes with Ethylene-Vinyl Acetate for Solution-Processed Conductive Films and Charge Extraction Layers in Perovskite Solar Cells. *ACS Appl. Mater. Interfaces* **2019**, *11*, 1185–1191. [CrossRef]
72. Yoon, S.; Ha, T.J.; Kang, D.W. Improving the performance and reliability of inverted planar perovskite solar cells with a carbon nanotubes/PEDOT:PSS hybrid hole collector. *Nanoscale* **2017**, *9*, 9754–9761. [CrossRef]
73. Lu, Y.; Zong, X.; Wang, Y.; Zhang, W.; Wu, Q.; Liang, M.; Xue, S. Noncovalent functionalization of hole-transport materials with multi-walled carbon nanotubes for stable inverted perovskite solar cells. *J. Mater. Chem. C* **2019**, *7*, 14306–14313. [CrossRef]
74. Ryu, J.; Yoon, S.; Park, J.; Jeong, S.M.; Kang, D.W. Fabrication of nickel oxide composites with carbon nanotubes for enhanced charge transport in planar perovskite solar cells. *Appl Surf Sci.* **2020**, *516*, 146116. [CrossRef]
75. Hu, X.G.; Lin, Z.; Ding, L.; Chang, J. Recent advances of carbon nanotubes in perovskite solar cells. *SusMat* **2023**, *3*, 639–670. [CrossRef]